the late 1960s. V_2O_3 with 3.75% Cr, for example, undergoes an insulator-metal transition under pressure and has a weakly positive Clapeyron slope, which terminates in a critical point at 1.25 GPa and 390 K (*16*). Structural studies have shown that the transition below T_c is isostructural and is associated only with a discontinuous change in lattice parameter. Furthermore, the conductivity first decreases with increasing temperature above T_c but then increases. This behavior was interpreted as a reentrant metallization that is continuous at high temperature with a negative Clapeyron slope (metallic phase above T_c) (*17*). This again may be similar to the behavior of hydrogen in the high-temperature, continuous metallization regime (*18*). Finally, we point out there is also recent evidence for analogous critical phenomena associated with pressure-induced isostructural insulator-metal transitions in other classes of materials (*19*).

REFERENCES AND NOTES

1. V. L. Ginzburg, *Key Problems in Physics and Astrophysics* (Mir, Moscow, 1978).
2. R. J. Hemley and H. K. Mao, *Phys. Rev. Lett.* **61**, 857 (1988).
3. H. K. Mao and R. J. Hemley, *Science* **244**, 1462 (1989).
4. R. J. Hemley and H. K. Mao, *Phys. Rev. Lett.* **63**, 1393 (1989).
5. H. K. Mao *et al.*, *ibid.* **65**, 484 (1990).
6. R. J. Hemley, H. K. Mao, J. F. Shu, in preparation.
7. E. Wigner and H. B. Huntington [*J. Chem. Phys.* **3**, 764 (1935)] originally predicted that hydrogen should transform to a monatomic metal under pressure. More recent theoretical studies have proposed that the molecular solid becomes metallic prior to this transition: D. E. Ramaker, L. Kumar, F. E. Harris, *Phys. Rev. Lett.* **34**, 812 (1975); C. Friedli and N. W. Ashcroft, *Phys. Rev. B* **16**, 662 (1977); B. I. Min, H. J. F. Jansen, A. J. Freeman, *ibid.* **33**, 6383 (1986); T. W. Barbee, A. Garcia, M. L. Cohen, J. L. Martins, *Phys. Rev. Lett.* **62**, 1150 (1989).
8. H. K. Mao, J. Xu, P. M. Bell, *J. Geophys. Res.* **91**, 4673 (1986); R. J. Hemley *et al.*, *Phys. Rev. B* **39**, 11820 (1989).
9. H. Lorenzana, K. A. Goettel, I. F. Silvera, *Phys. Rev. Lett.* **63**, 2080 (1989).
10. H. E. Stanley, *Introduction to Phase Transitions and Critical Phenomena* (Oxford Univ. Press, New York, 1971).
11. N. F. Mott, *Proc. Phys. Soc. A* **62**, 416 (1949); *Philos. Mag.* **6**, 287 (1961); *Metal-Insulator Transitions* (Taylor and Francis, London, 1974).
12. D. Jerome, T. M. Rice, W. Kohn, *Phys. Rev.* **158**, 462 (1967); B. I. Halperin and T. M. Rice, *Rev. Mod. Phys.* **4**, 755 (1968), and references therein.
13. We have found that extrapolation of the data obtained in the lower temperature range by Lorenzana *et al.* (*9*) also suggests that the vibron discontinuity may vanish at ~150 K. These authors did not discuss this result and its implication for critical behavior, however, possibly because their measurements were limited to lower temperatures and because they did not interpret the vibron transition as being associated with metallization.
14. We cannot yet rule out, for example, the possible formation of an excitonic insulator (*12*) stable at low temperatures over a narrow pressure interval as the band gap closes. The transition to such a phase (or phases) is also expected to exhibit critical behavior. Experimental verification of theses states appears incomplete, however (*19*).
15. The low-frequency rotational (or librational) bands (<400 cm^{-1}) have a weak dependence on temperature at these pressures. These results suggest the possibility of minor orientational transitions at higher temperatures that are distinct from the vibron transition (R. J. Hemley and H. K. Mao, in preparation).
16. D. B. McWhan and J. P. Remeika, *Phys. Rev. B* **2**, 3734 (1970); A. Jayaraman *et al.*, *ibid.*, p. 3751.
17. J. M. Honig and J. Spalek, *Proc. Indian Natl. Acad.* **52**, 232 (1986); J. Spalek, A. Datta, J. M. Honig, *Phys. Rev. Lett.* **59**, 728 (1987).
18. The metallization need not be strictly reentrant if there is a single high-pressure metallic phase. Although there may be a close parallel between the insulator-metal transition in hydrogen and in the doped V_2O_3 systems, we point out that there is evidence for three low-temperature phases in the latter [anti-ferromagnetic insulator, paramagnetic insulator, and paramagnetic metal (*16, 17*)]. The presence of the magnetic impurities and non-stoichiometry in the V_2O_3 alloys are likely to make insulator-metal transitions in this system more complex.
19. See for example, J. Neuenschwander and P. Wachter, *Phys. Rev. B* **41**, 12693 (1990), and references therein.
20. We thank J. Shu and M. Hanfland for help with the experiments, and N. W. Ashcroft for useful discussions. This work was supported by the NSF (grants EAR-8610086, EAR-8720320, and DMR-8912226), NASA (grant NAGW1722), and the Carnegie Institution of Washington.

25 May 1990; accepted 5 July 1990

Diffraction from Polymerized Membranes

FARID F. ABRAHAM AND DAVID R. NELSON

Flexible polymerized membranes in a good solvent are expected to exhibit a remarkable low-temperature flat phase, characterized by a diverging bending rigidity, vanishing elastic constants, and large fluctuations both parallel and perpendicular to the surface. A theory of the equilibrium structure factor provides a good fit to extensive molecular dynamics simulations of simplified "tethered surface" models of these materials. These results show how information about the size, thickness, and internal structure of polymerized membranes can be extracted from diffraction experiments.

TWO-DIMENSIONAL POLYMERIZED networks appear naturally in a biological context (*1*), and can be made artificially by, for example, modifying traditional methods of polymer synthesis, or by polymerizing ampiphillic bilayers or monolayers (*2*). A dilute solution of flexible sheet-like macromolecules prepared in this way should have properties which are strikingly different from conventional linear polymer chains. Polymer chains in a good solvent crumple into a fractal object whose characteristic size or "radius of gyration" R_g varies as a nontrivial power of the linear dimension L, $R_g \sim L^{3/5}$ (*3*). Linear polymers fold up on scales larger than a "persistence length" which is typically only a few monomer units in size. The statistical mechanics of two-dimensional polymer networks (*4*) has attracted intense theoretical interest, in part because, unlike linear polymers, they are expected to exhibit a low-temperature flat phase with an *infinite* persistence length. The flat phase arises because the resistance to in-plane shear deformations leads to an anomalous stiffening of the surface in the presence of thermal fluctuations (*5*). This flattening results from a delicate interplay between geometry and statistical mechanics which has no analog in conventional polymer solutions.

The simplest model of polymerized membranes is a "tethered surface," composed of hard spheres of diameter d each tied to six near neighbors to form a planar triangulated network; the network is then equilibrated at a finite temperature by allowing it to bend and possibly crumple in three dimensions. Although the first simulations of such tethered surfaces were interpreted in terms of a high-temperature crumpled phase (*4*), extensive simulations of much larger surfaces with a very similar potential revealed that these objects were in fact flat (*6, 7*), with very large fluctuations in the direction parallel to the average surface normal (see Fig. 1).

The elastic properties of this flat phase are embodied in an unusual long wavelength Hamiltonian which describes the energy of in-plane and out-of-plane phonon modes. In-plane phonon displacements $\mathbf{u}(x_1, x_2)$ and an out-of-plane displacement $f(x_1, x_2)$ are defined by the equation

$$\mathbf{r}(x_1, x_2) = m_0[(x_1 + u_1)\hat{\mathbf{e}}_1 + (x_2 + u_2)\hat{\mathbf{e}}_2 + f(\hat{\mathbf{e}}_1 \times \hat{\mathbf{e}}_2)] \qquad (1)$$

which gives the three-dimensional position vector $\mathbf{r}(x_1, x_2)$ of an atom in the membrane as a function of internal membrane coordinates x_1 and x_2 attached to the monomers. These internal parameters multiply orthogonal unit vectors $\hat{\mathbf{e}}_1$ and $\hat{\mathbf{e}}_2$ which span a flat zero temperature reference state (typically, a hexagonal piece of triangular lattice in computer simulations) of characteristic linear dimension L. Distances will be measured in units of d, the average spacing between nearest neighbor monomers in the reference

---

F. F. Abraham, IBM Research Division, Almaden Research Center, 650 Harry Road, San Jose, CA 95120-6099.
D. R. Nelson, Lyman Laboratory of Physics, Harvard University, Cambridge, MA 02138.

state. In Fig. 1, we present a top and side view of a particular configuration of a large simulated membrane, illustrated by drawing the tethered bonds between the 4219 monomers. The order parameter m_0 measures the shrinkage of the surface caused by thermal fluctuations (*8*). The probability of a particular surface configuration is proportional to $\exp(-H_{\mathrm{eff}}/k_B T)$, where the effective Hamiltonian, expressed in terms of the Fourier transformed phonon variables $\mathbf{u}(\mathbf{q})$ and $f(\mathbf{q})$, is

$$H_{\mathrm{eff}} = \frac{1}{2}\int \frac{d^2q}{(2\pi)^2}\left\{\kappa^{R}(q)q^4|f(\mathbf{q})|^2 + \mu_R(q)q^2|\mathbf{u}(\mathbf{q})|^2 + [\mu_R(q) + \lambda_R(q)]|\,\mathbf{q}\cdot\mathbf{u}(\mathbf{q})|^2\right\} \tag{2}$$

Unlike the conventional elastic theory of thin plates (*9*), the renormalized wave vector–dependent bending rigidity $\kappa_R(q)$ and in-plane elastic parameters $\mu_R(q)$ and $\lambda_R(q)$ are singular for small q (*5, 10*). The bending rigidity diverges according to the expression (*5, 10*).

$$\kappa_R(q) \sim \frac{1}{q^{2-2\zeta}} \tag{3}$$

while the elastic constants vanish as q tends to zero (*10*)

$$\mu_R(q),\ \lambda_R(q) \sim q^{\omega} \tag{4}$$

The exponent ζ determines how the membrane thickness $\langle f^2\rangle^{1/2}$ scales with L (*5, 11*), $\langle f^2\rangle^{1/2} \sim L^{\zeta}$. As shown by Aronovitz and Lubensky, the exponents ζ and ω are not independent, but obey instead the important scaling relation (*10*)

$$\zeta = \frac{1}{4}(2 + \omega) \tag{5}$$

The same result follows from a straightforward generalization of the integral equation for $\kappa_R(q)$ derived by Nelson and Peliti (*5*).

In this report we study the structure function associated with tethered surfaces in the flat phase. The structure function (see below) is closely related to the spatial Fourier transform of the monomer positions in a polymerized membrane; it can be measured experimentally via light, x-ray, or neutron diffraction. We calculate the structure function associated with the coarse-grained phenomenological model of the flat phase sketched above, and show that it provides a good description of extensive molecular dynamics simulations of tethered models. We measure the exponents ζ and ω and verify that they satisfy Eq. 5. Our results show how important information about the internal structure of real polymerized membranes can be extracted from diffraction experiments on both oriented and unoriented samples.

We first address the issue of why triangulated tethered surfaces are flat (*6*). The isotropic tethering potentials of Kantor *et al.* (*4*) and Abraham *et al.* (*6*) lead to very flexible membranes with no explicit microscopic bending rigidity. A priori, one might have expected such surfaces to crumple (*4*). One natural explanation of the results of Abraham *et al.* (*6*) is that a bending rigidity proportional to temperature is generated for entropic reasons by excluded volume interactions, even if there is no such term in the microscopic Hamiltonian (*11*). In fact, such a term is generated immediately upon introducing next nearest neighbor excluded volume constraints into a tethered network. A systematic study of the effects of reducing this rigidity by punching holes in the membrane (*12*) is currently under way (*13*). It is possible that gel-like tethered surfaces with sufficiently large perforations will be in the crumpled phase. The spectrin protein skeleton of erythrocytes (*1*), separated from its natural lipid environment and in a solution with a short Debye screening length, would be an excellent candidate for such a membrane. Adding an explicit bending rigidity to a triangulated network (*4*), but with a negative sign to partially compensate for the positive entropic contribution, could also lead to a crumpling transition.

In the remainder of this report, we concentrate on simple triangulated membranes in the flat phase. Our simulations were as described elsewhere (*6*), carried out on hexagonal sheets excised from a triangular lattice containing L monomers along the diagonal (*14*). The total number of monomers is $N = (3L^2 + 1)/4$. Figure 2 shows the structure function for an oriented membrane with $L = 49$ (that is, 1801 monomers). This structure function is defined by

$$S(q_z, q_\perp, L) = \frac{1}{N^2}\sum_{\underset{\sim}{x},\underset{\sim}{x}'}\left\langle e^{i\mathbf{q}\cdot[\mathbf{r}(\underset{\sim}{x}) - \mathbf{r}(\underset{\sim}{x}')]}\right\rangle = \frac{1}{N^2}\sum_{\underset{\sim}{x},\underset{\sim}{x}'}\left\langle e^{iq_z[r_z(\underset{\sim}{x}) - r_z(\underset{\sim}{x}')]} \times J_0(q_\perp|\mathbf{r}_\perp(\underset{\sim}{x}) - \mathbf{r}_\perp(\underset{\sim}{x}')|)\right\rangle \tag{6}$$

where $r_z(\underset{\sim}{x})$ is the monomer coordinate along the direction of the smallest eigenvalue of the moment of inertia tensor, and $\mathbf{r}_\perp(\underset{\sim}{x})$ is the corresponding perpendicular component. The z-axis is thus aligned with the average normal to the surface; the brackets indicate both a thermal average and an average over directions perpendicular to $\hat{z}$. Experimental realizations of oriented tethered surfaces are possible by, for instance, confining membranes between parallel glass plates.

The structure function displayed in Fig. 2 is remarkable, because of the nontrivial power law dependence along the q_z-axis and because of the distinctive oscillations in the shoulder along the $q_\perp$-direction. To understand this behavior, we must first measure the exponents ζ and ω. We can determine

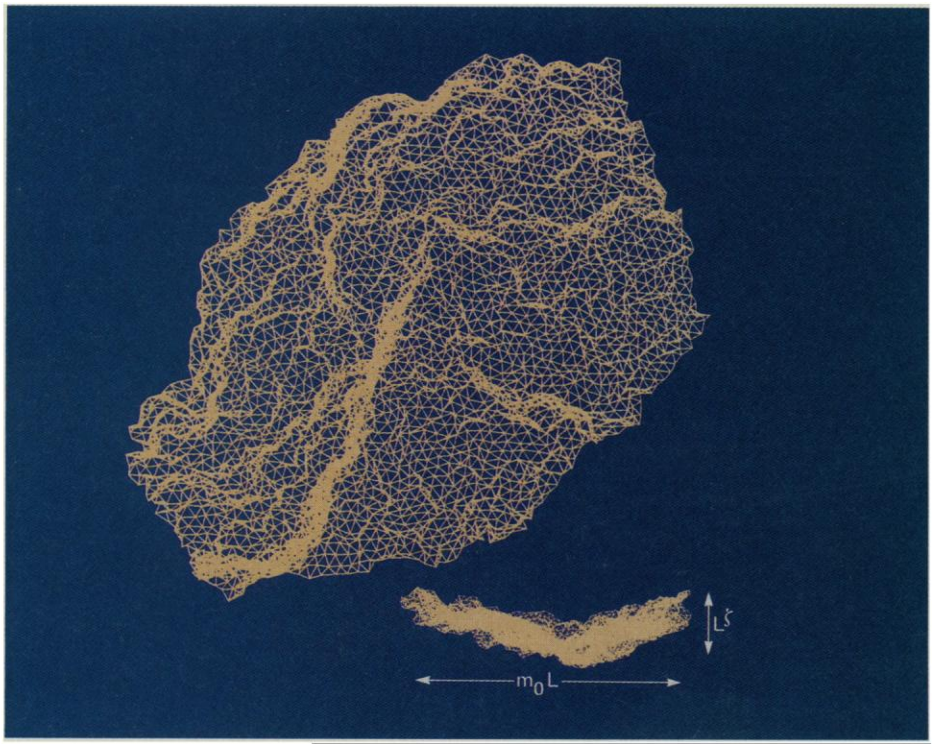

Fig. 1. A perspective and side view of an instantaneous configuration of a large tethered membrane composed of 4219 monomers.

the thickness exponent ζ from a log-log plot of $S(q_z, 0, L) \equiv \Phi(qL^\zeta)$ for a variety of values of L (see Fig. 3). The data for different L-values collapses when plotted versus qL^ζ, with $\zeta \approx 0.65$, in rough agreement with earlier estimates (*7, 8, 11*) of the membrane thickness exponent, but somewhat smaller than the result $\zeta = 0.8$ quoted by Abraham *et al.* (*6*) and based on the dependence between the smallest eigenvalue of the moment of inertia tensor and the membrane size. The value $\zeta = 0.65$ is consistent with the scaling prediction (*4*) $\Phi(x) \sim 1/x^{2/\zeta}$ for large x. Note from Fig. 3 that the crossover to this asymptotic behavior happens only for very large surfaces; the correct asymptotic behavior is not evident in the scaling plots of the smaller surfaces studied by other researchers (*7*).

To determine the exponent ω, we have plotted the mean squared in-plane monomer coordinate $\langle r_\perp^2 \rangle$ (measured relative to the center of mass) versus the squared internal distance of the monomer from the center of membrane. From Eq. 1 we expect that

$$\langle r_\perp^2(\underset{\sim}{x}) \rangle = m_0^2 x^2 + m_0^2 \langle u^2 \rangle \tag{7}$$

As shown in Fig. 4, plots for different L values are indeed linear (*15*). The intercepts determine $\langle u^2 \rangle$ which, upon using Eq. 2 to evaluate the average, is expected to scale like L^ω. A fit to compact membrane data for L = 13, 25, 49, and 75 gives $\omega = 0.66$. Inserting this result into the scaling relation Eq. 5 we find $\zeta = 0.67$, in very good agreement with our earlier result $\zeta = 0.65$.

These exponents allow us to compute the structure function displayed in Eq. 6. The decomposition (*1*) leads to

$$S(q_z, q_\perp, L) = \frac{1}{N^2} \sum_{\underset{\sim}{x}, \underset{\sim}{x}'} e^{i\mathbf{q}_\perp \cdot m_0(\underset{\sim}{x} - \underset{\sim}{x}')} \times \exp\left[-\frac{q_z^2}{2} \langle [r_z(\underset{\sim}{x}) - r_z(\underset{\sim}{x}')]^2 \rangle\right] \times \exp\left[-\frac{m_0^2}{2} q_{\perp i} q_{\perp j} \langle [u_{\perp i}(\underset{\sim}{x}) - u_{\perp i}(\underset{\sim}{x}')] \times [u_{\perp j}(\underset{\sim}{x}) - u_{\perp j}(\underset{\sim}{x}')] \rangle\right] \tag{8}$$

where $i, j = x, y$.

Upon using Eqs. 3 and 4, we find that the exponentiated averages must take the form

$$\langle [r_z(\underset{\sim}{x}) - r_z(\underset{\sim}{x}')]^2 \rangle \approx A|\underset{\sim}{x} - \underset{\sim}{x}'|^{2\zeta} \tag{9}$$

and

$$m_0^2 [u_{\perp i}(\underset{\sim}{x}) - u_{\perp i}(\underset{\sim}{x}')][u_{\perp j}(\underset{\sim}{x}) - u_{\perp j}(\underset{\sim}{x}')]\rangle \approx |\underset{\sim}{x} - \underset{\sim}{x}'|^\omega \times \left[B\left(\delta_{ij} - \frac{q_{\perp i} q_{\perp j}}{q_\perp^2}\right) + B' \frac{q_{\perp j} q_{\perp j}}{q^2}\right] \tag{9'}$$

where the coefficients A, B, and B' depend on the coefficients in Eqs. 3 and 4. We shall take $B = B'$ for simplicity, although this assumption is easily relaxed. Upon taking the continuum limit in Eq. 8 and replacing the hexagonal integration domains by disks of diameter L, we find

$$S(q_z, q_\perp, L) = \frac{16}{\pi} \int_0^1 ds\, s\left[\cos^{-1} s - s\sqrt{1 - s^2}\right] e^{-\frac{1}{2}(b_1 q_z L^\zeta s^\zeta)^2} \times J_0(b_2 q_\perp L s) e^{-\frac{1}{2} B(q_{\perp j} L^{\omega/2} s^{\omega/2})^2} \tag{10}$$

where $J_0(x)$ is a Bessel function. The parameters b_1 and b_2 are fixed by the behavior of the structure function for small q,

$$S(q_z, q_\perp, L) = 1 - \Lambda_z q_z^2 - \Lambda_\perp q_\perp^2 + O(q^4) \tag{11}$$

Λ_z is the smallest eigenvalue of the moment of inertia tensor

$$I_{\alpha\beta} = (1/2N^2) \sum_{\underset{\sim}{x}, \underset{\sim}{x}'} [r_\alpha(\underset{\sim}{x}) - r_\alpha(\underset{\sim}{x}')] \times [r_\beta(\underset{\sim}{x}) - r_\beta(\underset{\sim}{x}')] \tag{12}$$

while $\Lambda_\perp$ is the average of the remaining two eigenvalues. We then have

$$b_1 = \lim_{L \to \infty} \sqrt{\Lambda_z(L)/I_1 L^{2\zeta}}$$

and

$$b_2 = \lim_{L \to \infty} \sqrt{\Lambda_\perp(L)/I_2 L^2}$$

where

$$I_1 = \frac{8}{\pi} \int_0^1 ds\, s^{1 + 2\zeta} \times [\cos^{-1} s - s\sqrt{1 - s^2}] = 0.18644 \tag{13}$$

for $\zeta = 0.65$ and

$$I_2 = \frac{4}{\pi} \int_0^1 ds\, s^3 [\cos^{-1} s - s\sqrt{1 - s^2}] = \frac{1}{16} \tag{13'}$$

The remaining parameter B in Eq. 10 (or, more generally B and B', if Eq. 9 is used) must be fit to experiment.

The asymptotic large L structure function is determined once these parameters are known. We expect Eq. 10 to be accurate for all wavelengths large compared to typical monomer dimensions including, in particular, wavelengths large compared to either the transverse or in-plane membrane size. Although we do not expect Eqs. 9 to be reliable for $|\underset{\sim}{x} - \underset{\sim}{x}'| \lesssim d$ or $|\underset{\sim}{x} - \underset{\sim}{x}'| \approx L$, the factor $s[\cos^{-1} s - s\sqrt{1 - s^2}]$ deemphasizes these regions in Eq. 10.

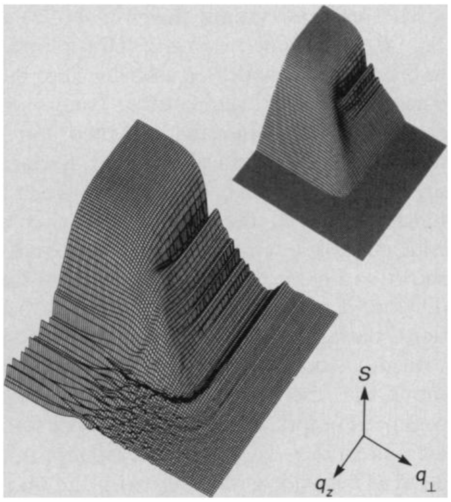

Fig. 2. The structure function $S(q_z, q_\perp, L)$ for an oriented compact membrane with $L = 49$ as measured from simulation (large surface) and calculated from theory (small surface). All scales are logarithmic as in Figs. 3 and 5.

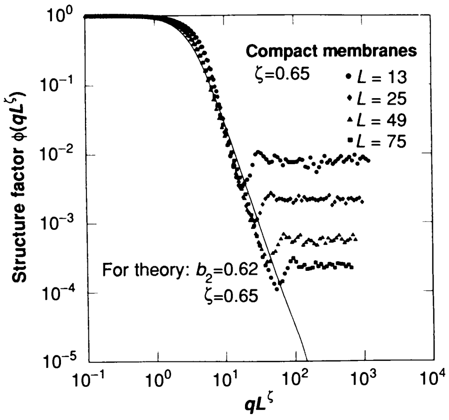

Fig. 3. The structure function for an oriented $S(q_z, 0, L) \equiv \Phi(qL^\zeta)$ versus qL^ζ for $\zeta = 0.65$ and for various values of L.

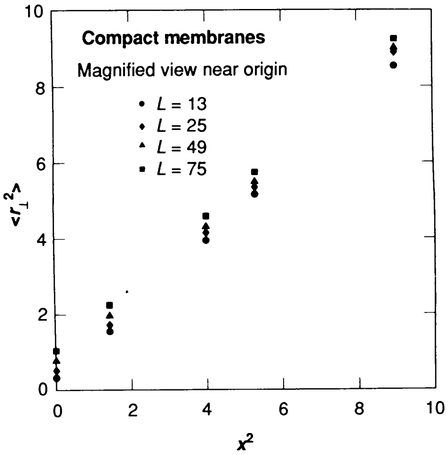

Fig. 4. The mean squared in-plane monomer coordinate $\langle r_\perp^2 \rangle$ (measured relative to the center of mass) versus the squared internal distance of the monomer from the center of membrane for the compact clusters.

The universal scaling function $\Phi(qL^{\zeta}) \equiv S(q_z, 0, L)$ obtained from Eq. 10 is plotted in Fig. 3, and provides a reasonable fit to the data. The fit is significantly better for $L = 49$ and 75. Note that the theory predicts a breakdown of scaling with L for **q** in the transverse direction: $S(0, q_\perp, L)$ is not a function only of the product $q_\perp L$ over a wide range of intermediate wave vectors. As shown in Fig. 5, the structure functions for different L exhibit L-independent oscillations starting at $q_\perp L \approx 10$, with the deepest oscillations occurring for large L. The inset shows that the theory (with B as a fitting parameter) captures this breakdown of scaling quite nicely. The physical reason for this peculiar behavior is the large in-plane phonon fluctuations: scaling is restored in Eq. 10 if we suppress these fluctuations by arbitrarily setting $B = 0$.

The inset to Fig. 2 shows the full theoretical prediction for $S(q_z, q_\perp, L)$ when $L = 49$. Although this hydrodynamic theory cannot describe the interesting structure in the simulation for $qd \gtrsim 1$, the overall shape and folds in the structure function are accounted for rather well.

Many laboratory experiments on tethered membranes will be carried out on unoriented membranes, and hence will be forced to deal with the a directionally averaged structure function $S(q, L)$. Even in this case, it may be possible to extract information about the size and structure of a polymerized membrane. A comparison of computer simulations with the theory for an $L = 49$ tethered surface averaged over different orientations is shown in Fig. 6. The kink which is barely discernible around $qL = 2\pi$ is a remnant of the first sharp dip in $S(0, q_\perp, L)$. For $2\pi L^{-1} < q < 2\pi L^{-\zeta}$, the membrane appears macroscopically flat and we would expect $S(q, L) \sim q^{-2}$. For $2\pi L^{-\zeta} < q < 2\pi d^{-1}$, the finite thickness of the membrane becomes evident and we expect $S(q, L) \sim q^{-2/\zeta}$. A region of slope -2 is evident beyond the kink in Fig. 6, and one can detect the beginning of a region with slope $-2/\zeta \approx -3.1$ just before the onset of the atomic scale oscillations. The two regimes become more evident when the theoretical curve is extrapolated to the much larger L-values (such as $L = 500$) which may soon become accessible in the laboratory.

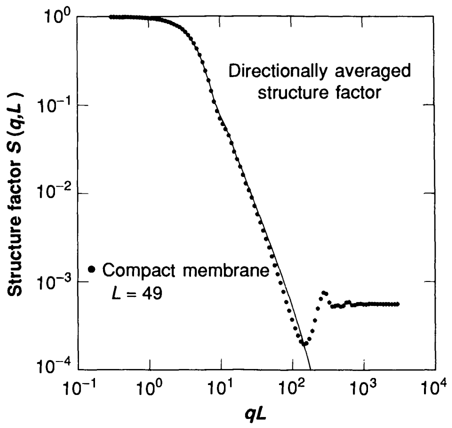

Fig. 6. The structure function of an unoriented compact membrane from simulation and theory.

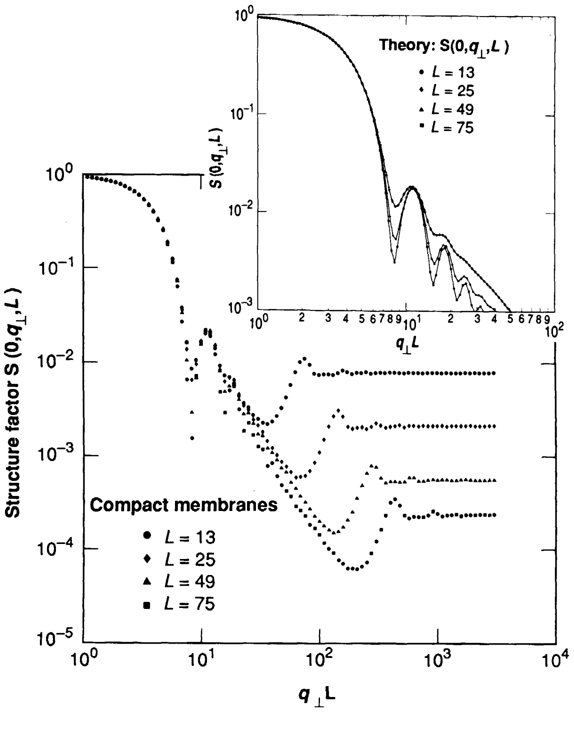

Fig. 5. The in-plane structure function $S(0, q_\perp, L)$ versus $q_\perp L$ over a wide range of L as measured from simulation and calculated from theory. The theoretical structure functions for $L = 13$ and 25 are indistinguishable in the plot.

We note that a closely related analysis applies to surfaces in the crumpled phase, where radius of gyration scales like $R_G \sim L^{\nu}$, with $\nu \approx 4/5$ (*4*). The structure function in this case assumes the form $S(q, L) = \Psi(qL^{\nu})$, where the scaling function is given by

$$\Psi(y) = \frac{16}{\pi}\int_0^1 ds\, s\left[\cos^{-1}s - s\sqrt{1-s^2}\right] \times \exp\left[-\frac{1}{2}(cy)^2\right] \qquad (14)$$

The scale factor c is determined by matching the small q expansion of Eq. 14 to the formula $S(q, L) = 1-(1/3)(qR_G)^2 + O(q^4)$.

A number of groups appear to be on the verge of systematic experimental studies of flexible polymerized membranes (*16*). By comparing computer simulation results to a simple theory of the structure function, we have shown here how information about the internal structure of the low-temperature flat phase can be extracted from standard diffraction experiments. The predictions are quite different from results expected for linear polymer chains; it would be very gratifying to see them tested in real laboratory experiments.

REFERENCES AND NOTES

1. B. Alberts *et al.*, *The Molecular Biology of the Cell* (Garland, New York, 1983). For a detailed discussion of spectrin, which behaves like a two-dimensional cross-linked gel at low temperatures, see A. Elgsaeter, B. Stokke, A. Mikkelsen, D. Branton, *Science* **234**, 1217 (1986).
2. A. Blumstein, R. Blumstein, T. H. Vanderspurt, *J. Colloid Interface Sci.* **31**, 236 (1969); S. L. Regen, J.-S. Shin, J. F. Hainfield, J. S. Wall, *J. Am. Chem. Soc.* **106**, 5756 (1984). N. Beredjick and W. J. Burlant, *J. Polymer Sci.* **A8**, 2807 (1970); J. H. Fendler and P. Tundo, *Acc. Chem. Res.* **17**, 3 (1984).
3. P.-G. deGennes, *Scaling Concepts in Polymer Physics* (Cornell Univ. Press, Ithaca, 1979).
4. Y. Kantor, M. Kardar, D. R. Nelson, *Phys. Rev. Lett.* **57**, 791 (1986).
5. D. R. Nelson and L. Peliti, *J. Phys. (Paris)* **48**, 1085 (1987).
6. F. F. Abraham, W. E. Rudge, M. Plischke, *Phys. Rev. Lett.* **62**, 1757 (1989).
7. For earlier speculations along these lines, see M. Plischke and D. Boal, *Phys. Rev. A* **38**, 4943 (1988); D. Boal, E. Levinson, D. Liu, M. Plischke, *ibid.* **40**, 3292 (1989). In our view, it is difficult to distinguish between the isotropic crumpling hypothesis of Kantor *et al.* (*4*) and the hypothesis of a flat, but very rough phase in these more modest simulations.
8. Y. Kantor and D. R. Nelson, *Phys. Rev. A* **38**, 4020 (1987).
9. L. D. Landau and E. M. Lifshitz, *Theory of Elasticity* (Pergamon, New York, 1970).
10. J. A. Aronovitz and T. C. Lubensky, *Phys. Rev. Lett.* **60**, 2634 (1988).
11. See, for example, S. Leibler and A. C. Maggs, *ibid.* **63**, 406 (1989).
12. We are indebted to S. Leibler for discussions on this point; In related work, G. S. Grest and M. Murat [*J. Phys. (Paris)*, in press] have studied randomly site-diluted tethered membranes, and find asymptotically flat surfaces in these randomly perforated surfaces. Such surfaces fall apart, however, beyond the percolation threshold.
13. F. F. Abraham and D. R. Nelson, in preparation.
14. Equilibration of these very large molecular dynamics simulations was described by Abraham *et al.* (*6*); similar results have been obtained in extensive recent Monte Carlo simulations by J.-S. Ho and A. Baum-

gärtner [*Phys. Rev. Lett.* **63**, 1324 (1989)], which increases our confidence that true thermodynamic equilibrium has been achieved.

15. This linearity breaks down far from the center, due to violent fluctuations of the membrane boundary. This boundary curls up significantly even in the flat phase, leading to contributions to a diffuse in-plane interface at this boundary which scale like L^{ζ} and $L^{\omega/2}$. See (*13*).
16. For a discussion of possible experiments, see D. R. Nelson, in *Statistical Mechanics of Membranes and Interfaces*, D. R. Nelson, T. Piran, S. Weinberg, Eds. (World Scientific, Singapore, 1989).
17. We thank W. E. Rudge for the graphics of Fig. 1. We have benefited from conversations with I. P. Batra, G. Grest, Y. Kantor, M. Kardar, and M. Plischke. Research by D.R.N. was supported by the National Science Foundation, through grant DMR88-17291 and through the Harvard Materials Science Laboratory.

6 March 1990; accepted 16 May 1990

Evolution of the Northern Santa Cruz Mountains by Advection of Crust Past a San Andreas Fault Bend

ROBERT S. ANDERSON

The late Quaternary marine terraces near Santa Cruz, California, reflect uplift associated with the nearby restraining bend on the San Andreas fault. Excellent correspondence of the coseismic vertical displacement field caused by the 17 October 1989 magnitude 7.1 Loma Prieta earthquake and the present elevations of these terraces allows calculation of maximum long-term uplift rates 1 to 2 kilometers west of the San Andreas fault of 0.8 millimeters per year. Over several million years, this uplift, in concert with the right lateral translation of the resulting topography, and with continual attack by geomorphic processes, can account for the general topography of the northern Santa Cruz Mountains.

ALTHOUGH THE GENERAL PATTERN of strain expected around restraining bends in strike-slip faults has long been known to result in uplift near the bend (*1*), the long-term dynamics of this uplift have rarely been documented. Strain patterns associated with strike-slip faults vary with the bend geometry, and with the slip distribution along the fault (*2*). Uplift rate maxima should coincide with the center of restraining bends, and die away from these bends in all directions. The combination of fault planes that accommodate the areal strain is not often known, however. As in the dip-slip fault case (*3*), a full model for the development of fault bend-related topography must necessarily include the patterns of coseismic uplift, interseismic relaxation, and geomorphic redistribution of mass. An added complexity in the strike-slip case results from the long-term advection of the evolving topography relative to the bend (*4*). The resulting topography rises in altitude when the local rate of uplift exceeds the rate of lowering due to geomorphic processes and decays when the geomorphic lowering dominates.

The Santa Cruz Mountains provide an excellent location for the study of fault bend dynamics because we may infer long-term uplift rates from well-dated marine terraces, the fault geometry and slip rates are well constrained, a recent seismic uplift event has occurred [the magnitude (M_S) 7.1 Loma Prieta earthquake of 17 October 1989 (*5*, *6*)] from which the coseismic uplift pattern may be inferred, and the geomorphic denudation rates are available. In this paper, I show that the time scales and magnitudes of the tectonic and geomorphic processes are consistent with the present topography of the Northern Santa Cruz Mountains. Both the topography that fits this simple picture, and that which does not, have implications for long-term slip rates, repeat times, the occurrence of other seismic events, and the longevity of bends in this reach of the San Andreas fault system.

Locally, the San Andreas fault (SAF; Fig. 1) slips at a rate of 12.2 ± 3.9 mm/yr (*7*, *8*). The fault bends at several different scales in the Santa Cruz Mountains (*9*). In the region between San Juan Bautista and the northern San Francisco peninsula the SAF describes a broad bend with a wavelength of 100 km (Fig. 1). This bend is accomplished by several shorter bends with divergence angles of 8° to 10° and wavelengths of ~10 km. One of these (10°) is centered north of Santa Cruz, the other at Black Mountain (8°) just west of Los Altos Hills (Fig. 1). The rupture associated with the Loma Prieta earthquake was centered about the first of these bends.

The Santa Cruz Mountains hug the SAF for ~100 km (Fig. 1). The fault crosses the middle of the mountain range in a prominent double restraining bend of approximately 3 km amplitude and 10 km length; the northern range occurs west of the fault and the southern range occurs to the east. The highest topography in the northern range (Mount Bielawski, 985 m) occurs near the northern edge of this bend, whereas

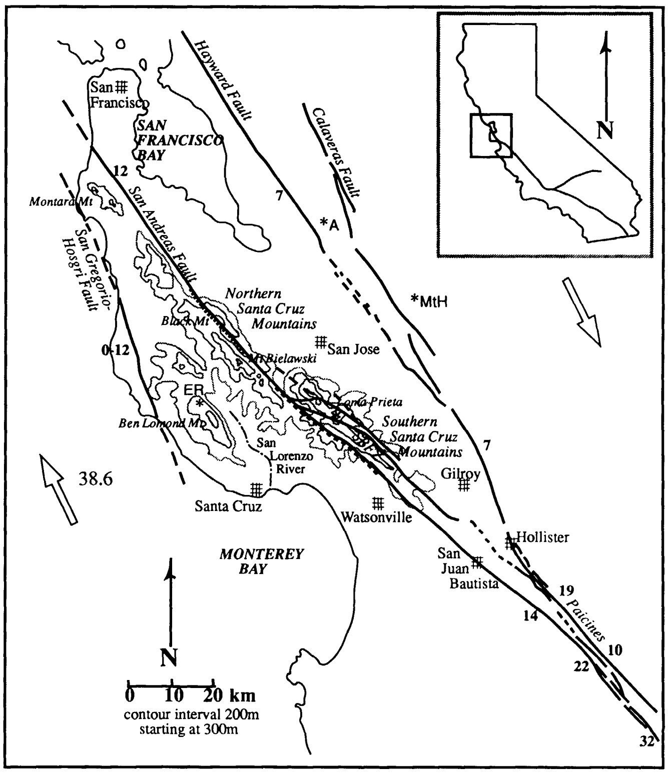

Fig. 1. Map of the Santa Cruz Mountains surrounding the slight bend in the San Andreas fault (SAF) in which the recent 17 October 1989 earthquake nucleated, as well as other major faults in the area (slip rates shown in millimeters per year; SBFZ, Sargent-Berrocal fault zone). Index map shows the SAF as it passes through California, and the Garlock fault. Note the broad bend in the SAF in the Monterey Bay region separating straight reaches of the fault. Smaller bends are the Santa Cruz bend, (long dashed) and the Black Mountain bend (short dashed). Topographic contours are shown at 200-m intervals starting at 300 m. Other topography (to the east of San Francisco Bay, and on the Monterey Peninsula) is not shown. Asterisks denote positions of geodetic stations occupied by the U.S. Geological Survey in the aftermath of the Loma Prieta earthquake.

Earth Sciences Board, University of California, Santa Cruz, CA 95064.